J Eng Math (2007) 58:177–189
DOI 10.1007/s10665-006-9123-5

ORIGINAL PAPER

Computations for large-amplitude two-dimensional body motions

Xinshu Zhang · Robert F. Beck

Received: 6 February 2006 / Accepted: 2 November 2006 / Published online: 1 December 2006

Abstract A numerical method is presented for the time-domain simulation of large-amplitude motions of a 2-D surface-piercing body with arbitrary shape in deep water. Based on potential theory, panels are distributed on the body and desingularized sources are distributed above the calm water surface. The body boundary condition is satisfied on the exact submerged body surface. The free-surface boundary conditions are linearized and satisfied on the calm water level. The solution is stepped forward in time by integrating the free-surface kinematic and dynamic conditions. The numerical solutions for the oscillation problem are compared with experimental results and other numerical results, and found to agree well. The results for the impact problem are compared with similarity solutions. Finally, results for the large-amplitude sinusoidal motion of a 45-degree wedge are presented.

Keywords Body-exact · Large amplitude · Water impact

1 Introduction

The accurate prediction of the wave-induced motions and loads is very important in ship and offshore design. Severe motions and extreme loads can lead to operability problems and in extreme cases structural failure and capsize. In the traditional approach to seakeeping calculations potential flow is assumed. The problem is linearized by assuming that the motions are small. The body boundary conditions are satisfied on the mean body surface and the free-surface conditions are linearized about the calm water level. The problem can be solved in either the time domain or the frequency domain because in linear potential-flow theory they are directly related by Fourier transforms. Linear system theory and random-process theory is then used to predict the extreme responses and loads. The primary objection to the linear system approach is that it often misses important features of extreme responses. For example, linear theory predicts that the hogging and sagging bending moments acting on a ship in a seaway have the same amplitude. In fact, due to nonlinearities, the hogging and sagging bending moments are significantly different. Another example is that linear theory (constant potential on the free surface) predicts that the vertical forces acting on a body entering or leaving the free surface have the same magnitude.

X. Zhang · R. F. Beck (✉)
Department of Naval Architecture and Marine Engineering, University of Michigan, Ann Arbor, MI 48109 USA
e-mail: rbeck@umich.edu

There are many variations to this linear approach. Strip theory (see [1]) is probably the most popular for long, slender ships. In this frequency-domain approach, the solution to the three-dimensional problem is approximated by solving a series of two-dimensional problems in the cross-flow plane. The two-dimensional problem is usually solved using a boundary-element method such as the one developed by Frank [2]. Frank's method uses constant-source-strength flat panels distributed over the mean submerged body contour. For offshore structures and more advanced ship-motion theories, 'panel methods' have been developed in which the mean wetted surface of the body is divided into panels and Green functions are used to solve the boundary-value problem. The free surface may or may not be panelized depending on whether a Rankine-source Green function or a free-surface Green function is used. For example, Prof. Newman and his students [3] have used the zero-speed free-surface Green function and higher-order panel methods to develop WAMIT, a code widely used in the offshore industry. A complete history of the various methods can be found in [4].

The other extreme from linear theory is to retain potential flow, but solve the fully nonlinear problem. In this case the body boundary condition is satisfied on the exact wetted surface of the body and the fully nonlinear free-surface boundary conditions are used. The computations are carried out in the time domain. The most common solution method is the mixed Euler-Lagrange, or MEL, method originally developed by Longuet-Higgins and Cokelet [5]. In this method, a linear mixed boundary-value problem is solved at each time step with the potential given on the exact free surface and the normal velocity is prescribed on the exact wetted surface of the body. The nonlinear free-surface boundary conditions are used to time step the potential on the free surface and the free-surface elevation. The body boundary condition is either known for forced motions or is determined by solving the dynamic equations of motion for the body. Many results are available in both two and three dimensions (see for example [6]). The problems with MEL computations are the instabilities of the free surface and wave breaking. The instabilities can often be eliminated by improved numerical techniques, but wave breaking is a natural phenomenon that is expected to occur in any large motion or wave situation. Computations normally are forced to stop when wave breaking occurs. Various techniques have been proposed to continue the computations after wave breaking, but they are not robust and can lead to nonphysical solutions.

A compromise between fully nonlinear computations and linear theory is the so-called double-body approach (see for example [7]). In this approach, the double-body flow is used to linearize the free-surface boundary conditions on a known surface (usually the calm water level, but it can be the incident wave surface). The body boundary conditions can be satisfied on either the mean wetted surface or the exact position. Wave breaking is no longer a difficulty because the free-surface boundary conditions are satisfied on a known surface. However, since free-surface Green functions no longer meet the free-surface boundary conditions, Rankine sources must be used and panels are distributed over both the body surface and the free surface. This in turn leads to difficulties on the edges of the computational domain and a large matrix inversion at each time step. The methods have shown improved seakeeping predictions, but computational costs preclude the method being used in preliminary design and optimization.

In order to develop computationally fast seakeeping calculations, but still retaining the important nonlinearities, blended methods in the time domain have been developed by several researchers (see for example the ISSC report [8], and [9]). Blended methods are a blend of linear and nonlinear approaches that have little rational basis. It is an engineering solution that combines the nonlinearities that are easily computed (the rigid-body equations of motion, the nonlinear hydrostatic force and the Froude–Krylov exciting force) with linear hydrodynamic computations for the radiation and diffraction forces. Typically, blended methods use linear theory to compute the radiation and diffraction forces acting on a two-dimensional section of the ship. Strip theory approximations are then used to determine the three-dimensional hydrodynamic forces. To improve the validity of blended method computations and still retain the high computational speeds that are necessary, we have developed a body exact technique. In this approach, the two-dimensional boundary-value problem is solved using an exact body boundary condition and a linearized free-surface boundary condition satisfied on the calm water surface. Similar to the fully nonlinear MEL computations,

at any time step the normal velocity is known on the exact body surface and the potential is given on the calm water level. The solution is time stepped using the known motions of the body and the linear free-surface conditions. As will be shown, the advantages of the method are that it introduces the nonlinearities associated with the change in wetted surface of the body, while retaining the computational efficiency of the linearized free-surface conditions. In addition, there are no breaking wave problems and numerical instabilities are minimized.

Another advantage of the present method is that it can deal easily with the water entry and exit problems, a situation that often exists in the bow and stern regions of high speed ships. The high pressures and impulse loads that occur during impact often set the structural design limits. Consequently, it is important that a blended method is able to assess rapidly these types of loads. The first classic work on the impact problem was due to von Kármán [10] who developed an asymptotic theory for the near-flat impact using a linearized body boundary condition and a constant potential free-surface condition. Wagner [11] went a step beyond von Kármán's solution by considering the effect of the water splash. Dobroboskaya [12] derived a similarity solution by using the geometric speciality of the body. The solution is valid only for small deadrise angles, and such a similarity solution does not exist for arbitrary bodies. Recently, Zhao and Faltinsen [13] used fully nonlinear free-surface simulations to predict the slamming loads. This fully nonlinear method includes the spray roots that are developed at the intersection of the body and free surface. However, it can not be used for a long time simulation due to wave breaking. It should be noted that the body-exact calculations in this paper neglect the details of the spray roots. As will be seen in Sect. 4.3, this can lead to an under-prediction of the impact force.

In this paper, we will first give the mathematical formulation followed by numerical techniques and convergence tests. Numerical results for various body shapes are given. It will be shown that the time-domain results agree with linear frequency-domain results for small amplitude motions. Nonlinear hydrodynamic forces are found for large-amplitude motions. Impact forces are examined for a wedge entering the water at high velocity and compared with other results. The problem of a body exiting from the water is also investigated. Contrary to linear theory, the hydrodynamic forces for the water-entry problem are found to be significantly different from those for the water-exit problem.

2 Mathematical formulation

We consider a general two-dimensional body floating on a free surface and undergoing arbitrary three-degree-of-freedom motions. An earth-fixed Cartesian coordinate system is chosen with the y-axis coincident with the quiescent free surface, and z-axis is positive upward. The fluid is assumed to be homogeneous, incompressible, inviscid and its motion is irrotational. Surface tension is neglected and the water depth is infinite. The fluid motions can be described by a velocity potential $\Phi(y, z, t)$. In the fluid domain, Φ satisfies the Laplace equation

$$\nabla^2 \Phi = 0. \tag{1}$$

On the mean free surface, the linearized free-surface boundary conditions are imposed

$$\zeta_t - \Phi_z = 0 \qquad \text{on } z = 0, \tag{2}$$

$$\Phi_t + g\zeta = 0 \qquad \text{on } z = 0, \tag{3}$$

where $z = \zeta(y, t)$ is the free-surface amplitude, and g is the acceleration due to gravity. On the *instantaneous* body boundary, no normal flux is permitted

$$\frac{\partial \Phi}{\partial n} = V_n \quad \text{on } S_b, \tag{4}$$

where the unit normal vector into the body $\mathbf{n}$ is positive out of the fluid; V_n is the instantaneous velocity in the normal direction including rotational effects. In the far field, the radiation boundary condition needs to be imposed that there are no incoming waves. The initial conditions at $t = 0$ are

$$\Phi = \Phi_t = 0 \quad \text{in the fluid domain.} \tag{5}$$

At each time step, a mixed boundary-value problem must be solved; the potential is given on the free surface and the normal derivative of the potential is known on the body surface. In terms of the desingularized sources above the calm water surface and sources distributed on the body surface, the potential at any point in the fluid domain can be given by

$$\Phi(\mathbf{x}) = \sum_{i=1}^{n} \sigma(\boldsymbol{\xi}_i) \log|\mathbf{x} - \boldsymbol{\xi}_i| + \int_{S_w} \sigma(\boldsymbol{\xi}) G(\mathbf{x}; \boldsymbol{\xi}) \mathrm{d}l, \tag{6}$$

where S_w represents the instantaneous wetted body surface and $|\mathbf{x} - \boldsymbol{\xi}_i|$ represents the distance between any point in the fluid domain and the desingularized source point. The function $G(\mathbf{x}; \boldsymbol{\xi})$ is a Rankine source Green function

$$G(\mathbf{x}; \boldsymbol{\xi}) = \log r, \tag{7}$$

$$r^2 = (y - \xi)^2 + (z - \eta)^2, \tag{8}$$

where r is the distance between a source point and a point in the fluid; $\boldsymbol{\xi}$ is the source point on the body boundary. Applying the boundary conditions, we obtain the integral equations that must be solved to determine the unknown source strengths are

$$\sum_{i=1}^{n} \sigma(\boldsymbol{\xi}_i) \log|\mathbf{x}_c - \boldsymbol{\xi}_i| + \int_{S_w} \sigma(\boldsymbol{\xi}) G(\mathbf{x}_c, \boldsymbol{\xi}) \mathrm{d}l = \Phi(\mathbf{x}_c) \quad \mathbf{x}_c \in \Gamma_d, \tag{9}$$

$$\sum_{i=1}^{n} \sigma(\boldsymbol{\xi}_i) \frac{\partial \log|\mathbf{x}_c - \boldsymbol{\xi}_i|}{\partial n} + \int_{S_w} \sigma(\boldsymbol{\xi}) \frac{\partial G(\mathbf{x}_c, \boldsymbol{\xi})}{\partial n} \mathrm{d}l = \chi(\mathbf{x}_c) \quad \mathbf{x}_c \in \Gamma_n, \tag{10}$$

where $\boldsymbol{\xi}$ = a source point
$\mathbf{x}_c$ = a point on the real boundary
χ = the given normal velocity on the body boundary
Φ = the given potential on the free surface ($z = 0$)
Γ_d = the free surface
Γ_n = exact submerged body surface.

Once the source strengths are found, Φ can be evaluated by (6), and the velocity on the body $\nabla\Phi$ can be obtained. The total pressure is given by Bernoulli's equation

$$p = -\rho\left(\frac{\partial \Phi}{\partial t} + \frac{1}{2}|\nabla\Phi|^2 + gz\right), \tag{11}$$

which can also be written as

$$p = -\rho\left(\frac{\delta \Phi}{\delta t} - V \cdot \nabla\Phi + \frac{1}{2}|\nabla\Phi|^2 + gz\right), \tag{12}$$

where $\frac{\delta\Phi}{\delta t}$ is the material derivative of Φ on a given global node and V is the moving 'node' velocity due to repanelization. In the present body-exact approach, we grid the body surface so that each panel has approximately the same length. The 'node' velocity can be calculated by using a backward-differencing scheme once we know the node position. The forces acting on the body can be obtained by integrating (12) over the instantaneous submerged body surface, which can be written as

$$\mathbf{F} = \int_{S_w} p\mathbf{n} \, \mathrm{d}l. \tag{13}$$

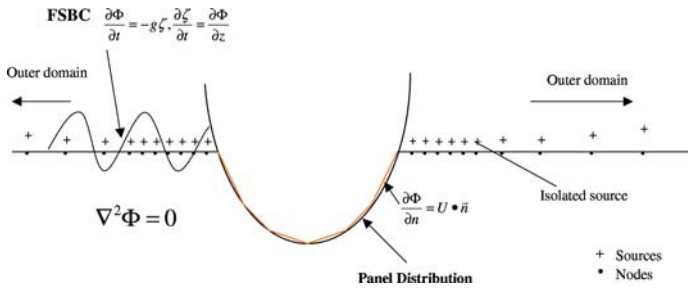

Fig. 1 Definition sketch

3 Numerical method

In the usual manner, the integrals shown in Eqs. 9 and 10 may be discretized to form a system of linear equations to be solved at each time step. As shown in Fig. 1, on the desingularized boundary, the sources are distribution outside the domain so that the source points never coincide with the collocation or node points and the integrals are nonsingular. In addition, because of desingularization, isolated sources are used rather than a source distribution. This greatly reduces the computation complexity of the influence matrix. The isolated sources are distributed a small distance above the calm water surface. The nondimensional desingularized distance is given by

$$L_{\mathrm{d}} = D_{\mathrm{m}}^{0.5}, \tag{14}$$

where D_{m} is the measure of the local mesh size, L_{d} is the desingularized distance. In order to resolve the leading-order radiated waves and minimize any wave reflection from the outer boundary, an inner and outer region is introduced in accordance with the work of Lee [14]. The inner domain spans eight wavelengths, with the body in the center. The wavelength is determined by the wave-dispersion relation $\lambda = 2\pi g/\omega^2$. Here ω is the oscillation frequency of the body. To properly resolve the radiated waves, 30 nodes per wave length are uniformly distributed over the inner domain. Near the intersection between the free surface and body, special care needs to be taken to match the size of the panels on the free surface and the body surface.

In order to prevent wave reflection and maintain continuity, numerical beaches are placed near the truncation boundaries. An additional 20 nodes are spread out over 80 wavelengthes beyond the inner domain. The spacing of these nodes increases exponentially from the constant spacing of the inner domain to the end of the outer domain. The spacing, in Eq. 15 was determined by Lee [14] to minimize the wave reflections.

$$\mathrm{d}x_{\mathrm{out}_i} = \mathrm{d}x_{\mathrm{in}} \times 1.0378^{\frac{i(i-1)}{2}}, \qquad i = 1 \ldots 20 \tag{15}$$

On the other hand, panels are distributed on the body surface. Panels are used because they are more suitable for any arbitrary body shapes than the desingularized sources. The integral equations (9) and (10) are satisfied at the nodes on the free surface and body surface such that

$$\sum_{j=1}^{N_F} \sigma_j^F \log|\mathbf{x}_{c_i}^F - \boldsymbol{\xi}_{s_j}^F| + \sum_{j=1}^{N_B} \sigma_j^B \int_{\Delta S_j} \log|\mathbf{x}_{c_i}^F - \boldsymbol{\xi}_j^B| \mathrm{d}l = \Phi\left(\mathbf{x}_{c_i}^F\right), \tag{16}$$

$$-\pi\sigma\left(\mathbf{x}_{c_i}^B\right) + \sum_{j=1}^{N_F} \frac{\sigma_j^F}{|\mathbf{x}_{c_i}^B - \boldsymbol{\xi}_{s_j}^F|} + \sum_{j=1, j\neq i}^{N_B} \sigma_j^B \int_{\Delta S_j} \frac{1}{|\mathbf{x}_{c_i}^B - \boldsymbol{\xi}_j^B|} \mathrm{d}l = \chi\left(\mathbf{x}_{c_i}^B\right), \tag{17}$$

where ΔS_j is the jth panel on the body surface. Equations 16 and 17 can be solved either by a direct or an iterative method depending on the size of the matrix. The LU decomposition method is used for calculations in this paper. Once the source strengthes are determined by solving the above equations, the fluid

velocity on the free surface can be computed. Then the free-surface elevation and the potential are updated by using the free-surface boundary conditions (2) and (3). The time stepping is accomplished using a 2nd-order Adams–Bashforth scheme as in Eqs. 18 and 19. The updated free-surface locations and potentials are then used to start the mixed boundary value problem at the next time step and the evolution continues.

$$\zeta(t+\triangle t) = \zeta(t) + \frac{\triangle t}{2}\left[3\left(\frac{\partial \zeta}{\partial t}\right)_t - \left(\frac{\partial \zeta}{\partial t}\right)_{t-\triangle t}\right], \tag{18}$$

$$\Phi(t+\triangle t) = \Phi(t) + \frac{\triangle t}{2}\left[3\left(\frac{\partial \Phi}{\partial t}\right)_t - \left(\frac{\partial \Phi}{\partial t}\right)_{t-\triangle t}\right]. \tag{19}$$

In order to ensure consistent free-surface resolution over time for the body-exact problem, the free-surface nodes are relocated to a distribution consistent with the original distribution relative to the current displaced body. This is accomplished by interpolating both ζ and Φ by a cubic spline for the newly distributed nodes.

The force acting on the body is evaluated by integrating the pressure over the instantaneous submerged surface using Eq. 13. The $\partial\Phi/\partial t$ on the body is evaluated by

$$\left(\frac{\partial \Phi}{\partial t}\right)_i^n = \frac{\delta \Phi_i}{\delta t} - V_i^n \cdot \nabla \Phi_i^n = \frac{\Phi_i^n - \Phi_i^{n-1}}{\Delta t} - \frac{\mathbf{X}_i^n - \mathbf{X}_i^{n-1}}{\Delta t} \cdot \nabla \Phi_i^n, \tag{20}$$

where Φ_i^n is the velocity potential of ith node at the nth time step on the body and V_i^n is the moving velocity of the grid points due to the repanelization on the body surface at each time step. When the panel number changes between time steps for extremely large motion amplitudes, Eq. 20 can not be used directly. Before the the $(j+1)$th time step when the panel number changes, the potential on the body nodes at the jth time step should be calculated again with the same panel number as at the $(j+1)$th time step. The recalculated potential will be used to calculate the pressure at the $(j+1)$th time step by using Eq. 20.

4 Results

4.1 Linear radiation problem

To verify the method, forced small-amplitude motions of a circular cylinder of radius R and a box ($B/T = 2.0$) are calculated including heave, sway, and roll motions. The body boundary condition is satisfied at the mean body position. The area of the circular cylinder section is A. The motion amplitude of the circular cylinder in heave and sway is $a = 0.1R$. The motion amplitude of the box in heave and sway is $a = 0.1T$. The motion amplitude of the box in roll is $a = 0.1\pi$. Once the force time histories are calculated, the added-mass and damping coefficients can be obtained by using Fourier analysis. The calculated added-mass and damping coefficients are compared with the experimental results of Vugts [15] and the results computed using a free-surface Green function (see for example [2]).

Figure 2 shows the convergence of the added mass of a circular cylinder both for the time step number in one time period and panel number on the body surface. The number of panels on the free surface remains essentially constant (i.e., 30 nodes per wavelength). For numerical accuracy, the first body panel must match the size of the first free-surface panel. Thus, as the number of body panels is increased, extra nodes must be added to the free surface in the vicinity of the body-free-surface intersection. The convergence curves suggest the good convergence characteristics of this method.

Figures 3 and 4 show the added mass and damping of the circular cylinder. Figures 5–7 show the added mass and damping of a box in heave, sway, and roll, respectively. For Figures 5–7, the panel number is $N = 40$ on the body surface, and the time step size $\triangle t$ is $T_{\text{period}}/100$. The comparisons shown in these figures are satisfactory and verify the accuracy of the present method for the linear problem.

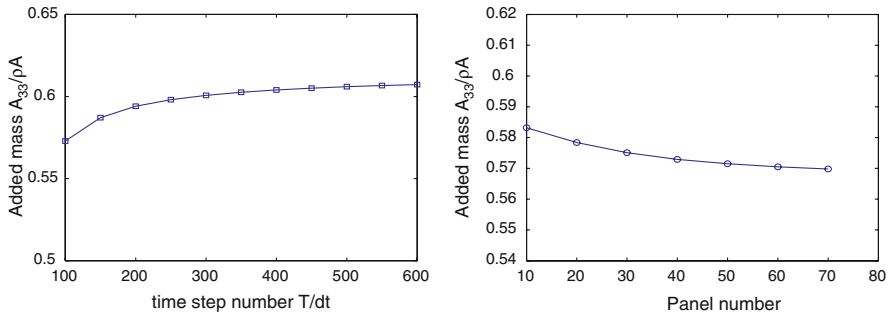

Fig. 2 Convergence of added mass of a circular cylinder in heave motion, $a = 0.1R$

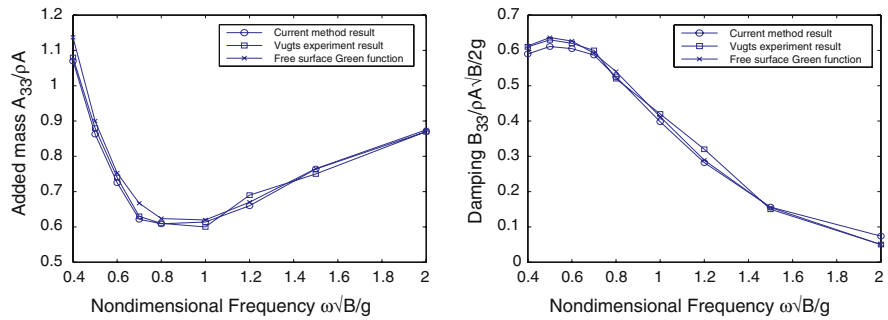

Fig. 3 Added-mass and damping coefficients of circular cylinder in heave motion

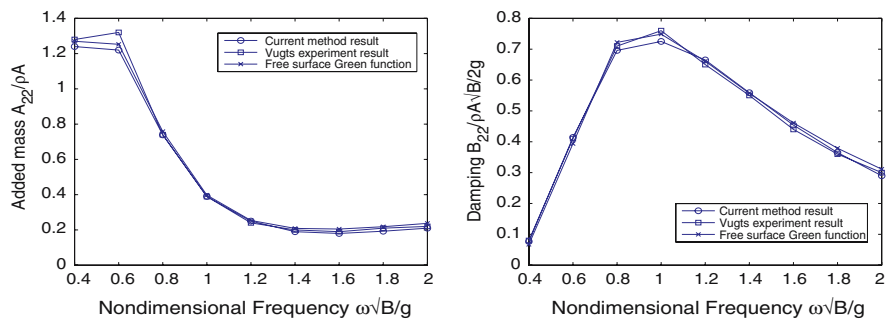

Fig. 4 Added-mass and damping coefficients of circular cylinder in sway motion

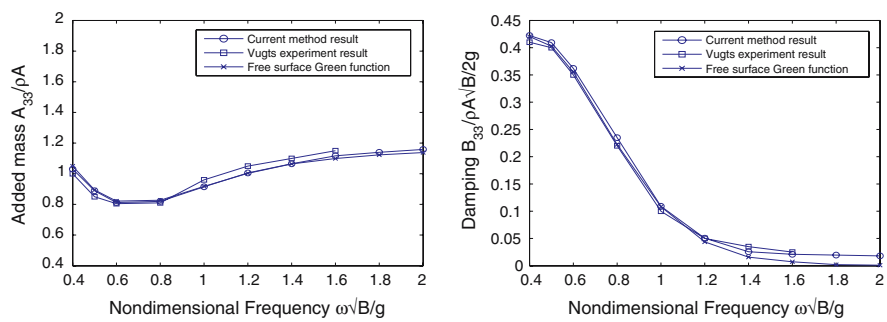

Fig. 5 Added-mass and damping coefficients of a box in heave motion

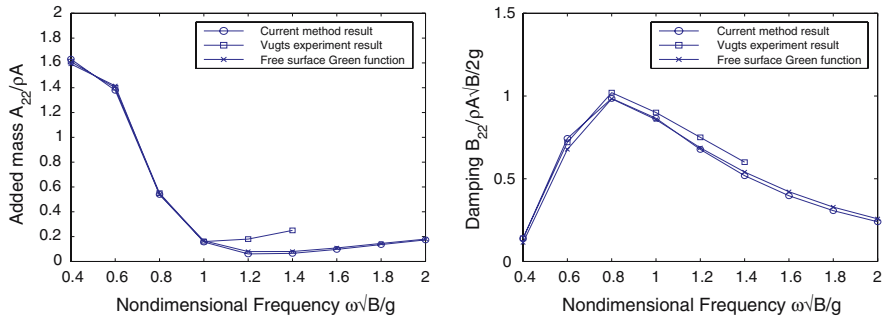

Fig. 6 Added-mass and damping coefficients of a box in sway motion

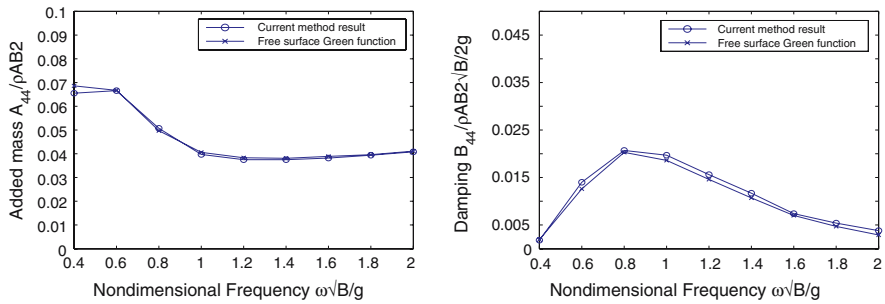

Fig. 7 Added-mass and damping coefficients of a box in roll motion

4.2 Body-exact problem

As an example, the forced large-amplitude motion of a circular cylinder of radius R is studied here. The cylinder is initially submerged such that the center is at the calm water line. The forced heave motion is $z(t) = -a \sin \omega t$, where a is the motion amplitude. We set $\omega R/g = 1.0$. Again, the panel number is $N = 40$ on the submerged body surface, and the time-step size $\triangle t$ is $T_{\text{period}}/100$. As addressed earlier, at each time-step, the submerged portion of the cylinder is repanelized, and the influence matrix is reevaluated.

Figure 8 shows the different components of the vertical force acting on the circular cylinder for the case of harmonic motion starting from rest with an amplitude of $a/R = 0.5$. The components correspond to each of the terms in Eq. 11. The steady state is rapidly reached. As shown, the hydrostatic force is the largest part of the force. The inertia term $\partial\Phi/\partial t$ shows a higher-harmonic component. In the computation, $\frac{\partial\Phi}{\partial t}$ is approximated by $(\frac{\delta\Phi}{\delta t} - V \cdot \nabla\Phi)$. The quadratic component $(-|\nabla\Phi|^2/2)$ is primarily a second-order harmonic.

The frequency components of the total force can be obtained by using Fourier analysis. The force coefficients are nondimensionlized according to Yamashita [16]

$$F_0^2 = \frac{|F(0)| - \rho g A_s}{2\rho g A^2}, \tag{21}$$

$$F_a^1 = \frac{|F(\omega)|}{2\rho g R A}, \tag{22}$$

$$F_a^2 = \frac{|F(2\omega)|}{2\rho g A^2}, \tag{23}$$

where $|F(\omega)|$ is the amplitude of the Fourier component of the force at that frequency and is determined using a Fourier transform. Here A_s is the mean submerged cross section area; F_0^2 is the second-order mean force; F_a^1 is the first-order harmonic force; F_a^2 is the second-order harmonic force.

For $a/R = 0.2$, the frequency components of the vertical force are given in normalized form in the Table 1. The values are compared with the experiments of Yamashita [16] and numerical results of Kent

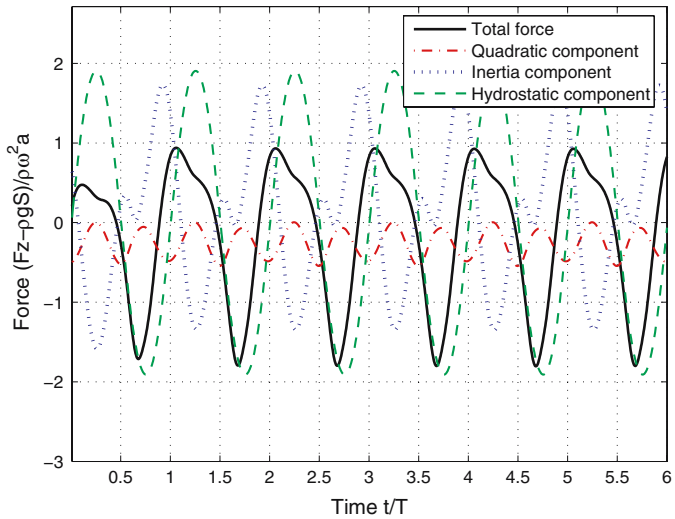

Fig. 8 Vertical force acting in the circular with $a = 0.5R$, $\omega^2 g/R = 1.0$

Table 1 Comparing frequency component amplitudes of the vertical force on circular for large-amplitude motion

$a/R = 0.2$	$\frac{\omega^2 R}{g}$	F_0	F_1	a_{33}	b_{33}	F_2
Yamashita (1977)	0.5	−0.01	/	0.66	0.72	0.15
Kent (2005)	0.5	−0.01	0.821	0.60	0.796	0.194
Present calculation	0.5	−0.013	0.815	0.63	0.82	0.163
Yamashita (1977)	1.0	−0.08	/	0.60	0.39	0.45
Kent (2005)	1.0	−0.086	0.615	0.58	0.375	0.491
Present calculation	1.0	−0.086	0.632	0.60	0.41	0.428
Yamashita (1977)	1.5	−0.15	/	0.69	0.22	0.8
Kent (2005)	1.5	−0.16	0.36	0.62	0.209	0.796
Present calculation	1.5	−0.19	0.378	0.67	0.23	0.62

[17] obtained by using a third-order pseudo-spectral method. The comparisons in Table 1 show good agreement for the mean force and the first-order force. Present calculations also capture the main part of second-order force. The agreement is surprisingly good considering only a linearized free-surface boundary condition is used. It also suggests that, in this case, the nonlinear effects associated with the geometry play a more important role than the wave nonlinearities.

4.3 Water-entry and -exit problem

The impact problem for 30, 45, and 60 degree wedges (where the angle is the apex included half-angle) was investigated. The pressures over the wedges and slamming forces were compared with the similarity solutions presented by Zhao and Faltinsen [13]. The similarity solution neglects gravity and uses a $\Phi = 0$ free-surface boundary condition. We have run our own calculation both with and without gravity in the free-surface condition. The initial conditions were set such that the wedges had negligible initial draft and a constant downward velocity of 10 meters-per-second. Figure 9 shows the effects of gravity on the computations, after the pressure distribution reaches steady state. As can be seen in Fig. 13, the transients die out quickly and steady state is reached after 0.05 seconds. As seen in Fig. 9, when the water-entry velocity is high enough, the effects of gravity are almost negligible. Also shown in Fig. 9 are results for a 'stretched' pressure distribution. As discussed for Figs. 10–12, resolving the pressure distribution only to $z = 0$ results in too small a vertical force. It is proposed to improve the solution by 'stretching' the wetted

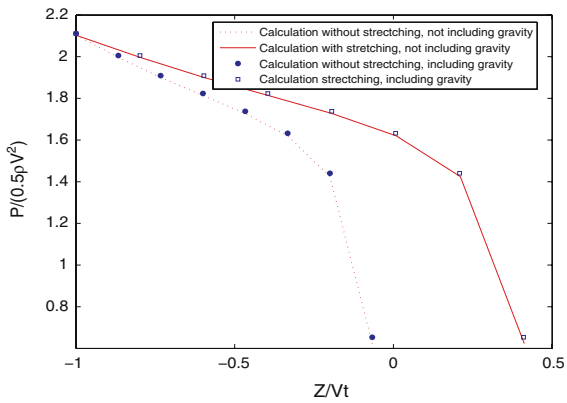

Fig. 9 Gravity effect on pressure distribution over a 45-degree wedge with large entry-water velocity

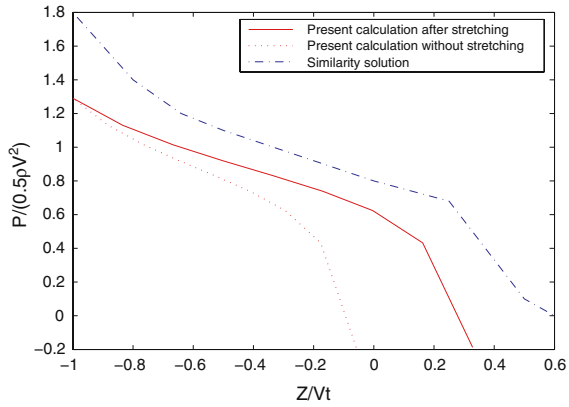

Fig. 10 Pressure distribution over a 30-degree wedge

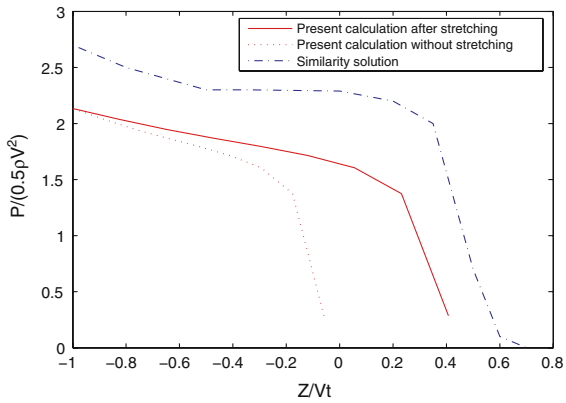

Fig. 11 Pressure distribution over a 45-degree wedge

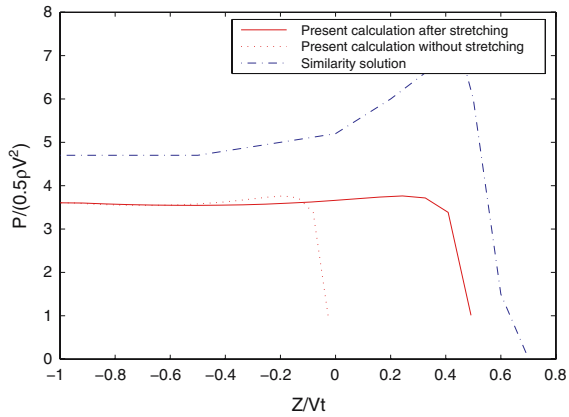

Fig. 12 Pressure distribution over a 60-degree wedge

surface. Using Eq. 3, the intersection of the free surface and the wedge can be calculated. Once the wetted surface is known, the pressure distribution can be stretched up to that point.

The pressure distributions on the wedges during impact are shown in Figs. 10–12 for wedges of 30, 45, and 60 degrees, respectively. As can be seen, there is significantly disagreement between the similarity solution of Zhao and Faltinsen [13] and the pressure distribution to $z = 0$. The stretched pressure distributions are also shown in Figs. 10–12. The agreement with the similarity solution is greatly improved. Figure 13 shows the impact force acting on a 45-degree wedge found by integrating the pressures. All these values are compared with the similarity solution, since as Fig. 9 shows the effects of gravity are small. As can be seen, the unstretched values in these figures are the smallest, which are very close to the von Kármán's solution, approximately half of the similarity solution. The comparisons also suggest that impact pressures and forces calculated using the stretching technique are much better than the unstretched results. While the agreement is not perfect, the results do show that this computationally fast, simplified model gives reasonable results.

Figures 14 and 15 show the force time history acting on a 45-degree wedge undergoing large-amplitude sinusoidal motion. The body enters the water at $t = 0$ s, and reaches the bottom of the down stroke at $t = 0.5$ s. At $t = 1$ s the body exits the water and remains out of the water until it re-enters at $t = 2$ s. The cycle then repeats itself. Figure 14 shows the force time history for a $\Phi = 0$ free-surface boundary

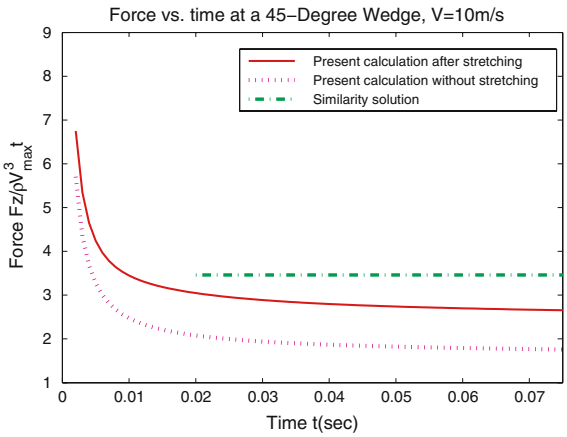

Fig. 13 Hydrodynamic impact force acting on a 45-degree wedge

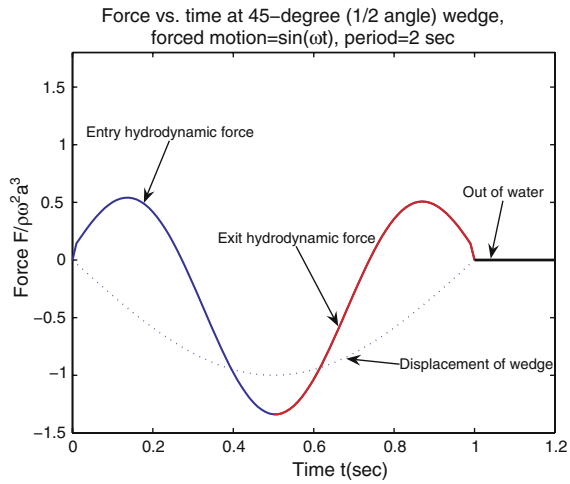

Fig. 14 Force acting on a 45-degree wedge in large-amplitude sinusoidal motion with $\Phi = 0$ at the free surface

Fig. 15 Force acting on a 45-degree wedge in large-amplitude sinusoidal motion with linearized free-surface boundary conditions

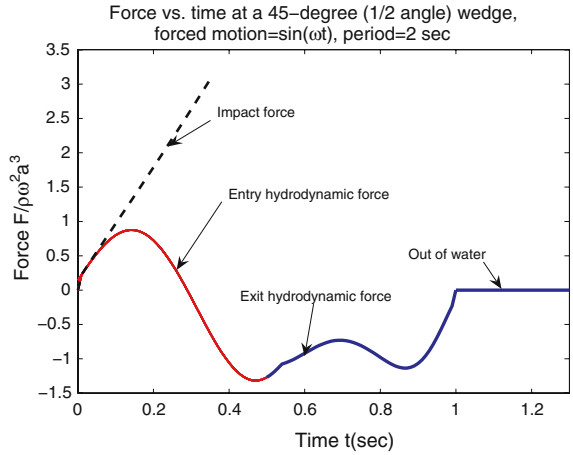

condition. This is the free-surface boundary condition normally used for the impact problem. The dashed curve shows the displacement of the wedge as a function of time. As can be seen, the exit force and entry force are identical. Figure 15 shows the force time history due to the same displacement time history as in Fig. 14, but using the linearized free-surface boundary conditions. On the water-entering phase of the motion, the stretching technique is applied. As the wedge starts to exit the water, the computed wave amplitude near the body reverses and becomes negative. The negative wave amplitude may become larger than the body draft. Consequently, the stretching is turned off as soon as the predicted wave amplitude near the body becomes negative. As shown in Fig. 15, for small times, the impact force is consistent with the water-entry problem. In addition, the shape of the entry force curve in Fig. 15 has the same form as in Fig. 14. However, the water-exit-force curve in Fig. 15 shows a significant difference from the exit-force curve in the $\Phi = 0$ problem (Fig. 14). The differences are due to the free-surface boundary conditions and the formation of free-surface waves.

5 Conclusions

Two-dimensional, large-amplitude body motion is studied in this paper with linearized free-surface and exact body boundary conditions. By distributing desingularized sources above the calm water surface and distributing panels on the body, the boundary-integral equation can be solved at each time step. The free-surface boundary conditions are integrated at each time step by using a second-order Adams–Bashforth scheme. The free surface and body surface are regrided after each time step due to a changing submerged body surface. Numerical results are obtained for small-amplitude motions of a circular cylinder and a box, large-amplitude motions of a circular cylinder, and water entry and exit of a wedge. The small-amplitude-motion results show that the present numerical model has good convergence for panel numbers and time step size. For the large-amplitude body-exact computations, present calculations agree very well with experiments and other numerical results for the first-order force. The predicted second-order forces also capture the main part of the experimental values. They indicate that the nonlinear free-surface effects are not important in this case, and the nonlinearities associated with the geometry may play a more important role.

For the wedge-impact problem, by comparing the numerical solution with and without gravity it was found that the gravity effects are very small when the impact velocity is large. This means that the similarity solution (i.e., no gravity) can be compared to the large-time asymptotics of the presented calculation. To make the comparisons, two techniques were used. In the first technique (no stretching), the resultant impact pressure distribution is integrated up to the equivalent calm water line. This is equivalent to the classical von Kármán's [10] solution from the wedge-impact problem. In the second technique (with stretching), the impact pressure distribution is 'stretched' up to the predicted intersection of the free surface and body surface. This is similar to Wagner's [11] approach of taking into account the wave rise on the body surface. In comparison with the similarity solution, the second technique gives much better answers. The first technique gives answers that were approximately $1/2$ of the stretched solution. Similar results are obtained when comparing von Kármán's solution to Wagner's solution.

Numerical results for a water-exit problem are also presented in this paper. Forces acting on a 45-degree wedge undergoing large-amplitude sinusoidal motions so that the wedge goes into and out of the water are calculated by using different free-surface boundary conditions. Using a $\Phi = 0$ free-surface boundary condition, the water-exit force and -entry forces are identical. For the case of linearized free-surface boundary conditions and stretching the wetted-surface pressure distribution, the entry water force is the same as that in the water-impact problem. However, the water-exit force shows a significant difference from that in the $\Phi = 0$ problem. The differences are due to the memory effects of free surface and the formation of the free-surface waves. Future work will address the extension to three-dimensional computations.

Acknowledgements The authors would like to express their appreciation to Prof. Troesch of the Naval Architecture and Marine Engineering Department for discussions regarding this work. This work was supported by Office of Naval Research, contracts N00014-04-1-0266 and N00014-05-1-0537.

References

1. Salvesen N, Tuck EO, Faltinsen O (1970) Ship motions and sea loads. Trans SNAME 78:250–287
2. Frank W (1967) On the oscillation of cylinders in or below the free surface of deep fluids. Naval Ship Res Develop Center Report No. 2375
3. Lee C-H, Newman JN (2004) Computation of wave effects using the panel method. In: Chakrabarti (ed) Numerical models in fluid-structure interaction. WIT Press, Southhampton
4. Beck RF, Reed AM (2001) Modern seakeeping computations for ships in seaway. SNAME Trans 109:1–52
5. Longuet-Higgins MS, Cokelet ED (1976) The deformation of steep surface waves on water: I. A numerical method of computation. Proc R Soc London Ser A A 350:1–26
6. Beck RF (1999) Fully nonlinear water wave computations using a desingularized Euler–Lagrange time-domain approach. In: Nonlinear Water Wave Interac WIT Press, pp 1–58

7. Sclavounos PD (1996) Computations of wave ship interactions. In: Ohkusu M (ed) Advances in marine hydrodyanmics. Computational Mechanics Publications, pp 233–278
8. Jensen J, Beck RF, Du S, Faltinsen O, Fonseca N, Rizzuto E, Stredulinsky D, Watanabe I (2000) Extreme Hull Girder Loading. Proceedings 14th International Ship and Offshore Structures Congress, Vol 2. Nagasaki, Japan, pp 236–320
9. Finn P, Beck RF, Troesch AW, Shin YS (2002) Nonlinear impact loading in an oblique seaway. J Offshore Mech Arctic Eng, 125(3):190–197
10. von Karman T (1929) The impact on seaplane floats during landing. NACA TN 321
11. Wagner H (1932) Über stoss- und gleitvergänge an der oberfläche von flüssigkeiten. ZAMM 12:193–215
12. Dobrovol'skaya ZN (1969) On some problems of similarity flow of fluid with a free surface. J Fluid Mech 36(part4):805–829
13. Zhao R, Faltinsen O (1993) Water entry of two-dimensional bodies. J Fluid Mech 246:593–612
14. Lee T-H (1992) Nonlinear radiation problems for a surface-piercing body. PhD. Thesis, Department of Naval Architecture and Marine Engineering, The University of Michigan, USA
15. Vugts JH (1968) The hydrodynamic coefficients for swaying, heaving and rolling cylinders on a free surface. Shipbuilding Laboratory, Technical University Delft, Report No. 112 S
16. Yamashita S (1977) Calculation of hydrodynamic forces acting upon thin cylinders oscillating vertically with large amplitude. J Soc Nav Arch No 141 Japan 61–70
17. Kent CP (2005) A pseudo-spectral method for calculating wave-body interaction using an explicit free-surface formulation. PhD. Thesis, Department of Naval Architecture and Marine Engineering, The University of Michigan